Valence-to-Core-Detected X-ray Absorption Spectroscopy: Targeting Ligand Selectivity

Eleanor R. Hall,[†,‡] Christopher J. Pollock,[†,∇] Jesper Bendix,[§] Terrence J. Collins,[||] Pieter Glatzel,[⊥] and Serena DeBeer*[,†,#]

[†]Max-Planck-Institut für Chemische Energiekonversion, Stiftstrasse 34-36, D-45470 Mülheim an der Ruhr, Germany

[‡]Department of Chemistry, University of Oxford, Oxford OX1 2JD, United Kingdom

[§]Department of Chemistry, University of Copenhagen, Universitetsparken 5, DK-2100 Copenhagen, Denmark

[||]Department of Chemistry, Carnegie Mellon University, Pittsburgh, Pennsylvania 15213, United States

[⊥]European Synchrotron Radiation Facility, 71 Rue des Martyrs, 38000 Grenoble, France

[#]Department of Chemistry and Chemical Biology, Cornell University, Ithaca, New York 14853, United States

S *Supporting Information*

ABSTRACT: X-ray absorption spectroscopy (XAS) can provide detailed insight into the electronic and geometric structures of transition-metal active sites in metalloproteins and chemical catalysts. However, standard XAS spectra inherently represent an average contribution from the entire coordination environment with limited ligand selectivity. To address this limitation, we have investigated the enhancement of XAS features using valence-to-core (VtC)-detected XAS, whereby XAS spectra are measured by monitoring fluorescence from valence-to-core X-ray emission (VtC XES) events. VtC emission corresponds to transitions from filled ligand orbitals to the metal 1s core hole, with distinct energetic shifts for ligands of differing ionization potentials. VtC-detected XAS data were obtained from multiple valence emission features for a series of well-characterized Mn model compounds; taken together, these data correspond to a VtC resonant XES (VtC RXES) plane. For comparison, standard total fluorescence yield (TFY) XAS and nonresonant XES data were obtained. Dramatic intensity variations and the appearance of new features were observed in the pre-edge region by detecting at different VtC emission energies. The TFY XAS, nonresonant XES, and VtC RXES data were all modeled within a density functional theory approach. While the TFY XAS and nonresonant XES data are readily interpreted by theory, the VtC RXES cannot be reproduced within such a simplified model. Nonetheless, dramatic changes in the experimental spectra are observed that have the potential to further the information content and selectivity of XAS. Potential applications and required theoretical developments are discussed.
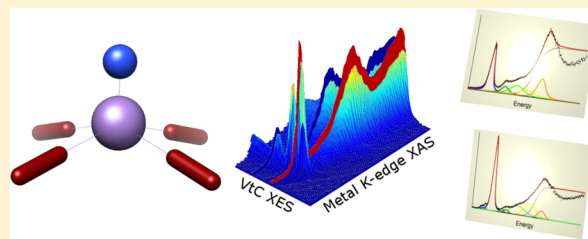
INTRODUCTION

Metal K-edge X-ray absorption spectroscopy (XAS) has long been used to probe the electronic and geometric structures of transition-metal complexes. The applicability of this technique to a wide range of sample environments has enabled the use of XAS on solid-state,[1,2] small-molecule,[3,4] and biological systems.[5–7] As transitions into unoccupied orbitals are involved, XAS features yield information about the geometric and electronic structures of transition-metal complexes. At the lowest energies, the pre-edge and near-edge regions [together termed the X-ray absorption near-edge structure (XANES) region] of the spectrum correspond to 1s to 3d (+4p) transitions. Arising from transitions into bound unoccupied orbitals, the XANES region is sensitive to the metal oxidation state and site symmetry. To higher energies lies the extended X-ray absorption fine structure (EXAFS) region that results from the ionized photoelectron scattering off the electrons of nearby atoms. Analysis of this region complements the edge and can provide metrical information about the ligands nearest the

metal center. Together, XANES and EXAFS have provided invaluable insights into the geometric and electronic structures of transition-metal complexes.[4,7]

The information provided by XAS is, however, an average of all metal–ligand interactions. Hence, for XANES data on an isotropic sample, specific metal–ligand contributions are challenging or impossible to deconvolute. Using polarized single-crystal measurements, however, one can separate out specific metal–ligand contributions to the XANES spectra.[8,9] This has been previously demonstrated for Mn(V) oxo and nitrido complexes, where alignment of the X-ray **e** vector along the short Mn–N and Mn–O bonds allowed for isolation of the nitrido and oxo contributions, respectively, from the remaining coordinated light atoms.[10] However, the requirement for single crystals greatly limits the applicability of polarized XAS. The separation of ligated light atoms (e.g., C, N, or O) is also a well-

known limitation of EXAFS analysis. Chemically, though, it is very often desirable to separate out specific metal–ligand contributions, particularly in complex media—such as metal catalysts—where one may want to select for a specific substrate at a specific stage of a chemical transformation.

One possibility for obtaining ligand selectivity in complex media, initially proposed by de Groot in 2001,[11] is to use a high-resolution X-ray emission spectrometer to detect XAS using valence-to-core X-ray emission (VtC XES) transitions. These so-called high-energy-resolution fluorescence detection (HERFD) schemes should provide ligand selectivity by exploiting the known sensitivity of the VtC region to the ligand electronic structure. In particular, the low-energy Kβ″ feature is known to be diagnostic for the ns orbital ionization potential of atoms bound to a metal center: more than 8 eV separates the features from fluoride, oxide, and nitride donors,[12–15] and even differing protonation patterns of the same atom can be identified.[14,16,17] Hence, the VtC region is ideal for the detection of XAS spectra that are selective for a given ligand.

The first demonstration of HERFD measurements was conducted by Hämäläinen and co-workers.[18] In this study, the authors observed dramatic sharpening of the dysprosium L_3 edge, including the appearance of new features that were unresolved in the transmission spectrum, by detecting from the $L\alpha_1$ emission line. While detecting from this particular core-to-core XES transition did not confer any chemical selectivity to the XAS spectrum, it demonstrated the feasibility and resolution enhancements available via HERFD.

Following this report, applications of HERFD to transition-metal complexes expanded rapidly.[19–22] The $K\alpha$ lines (i.e, 2p to 1s emission features) are highly intense features that are an attractive target for HERFD detection. However, as $K\alpha$ emission corresponds to deep core-to-core transitions on the metal, they are rather insensitive to changes in the ligation sphere. $K\alpha$ lines do possess a modest sensitivity to the metal spin state,[23] though neither the $K\alpha_1$ nor $K\alpha_2$ line corresponds to a "pure" high- or low-spin final state. In contrast, the $K\beta$ lines have significant oxidation and spin-state sensitivity for 3d transition metals.[12,24,25] It was shown that spin-selective XAS spectra could be obtained using $K\beta$ HERFD by detecting from either the $K\beta_{1,3}$ or $K\beta'$ features of complexes with high-spin d^5 metal centers.[19,21,22] Furthermore, the spin sensitivity of the $K\beta$ main line was exploited to obtain chemically selective EXAFS for the two distinct iron sites in Prussian blue.[26] Together, these experiments affirmed that new information may be obtained by detecting XAS spectra from different emission features. In principle, even greater selectivity should be achieved by detecting XAS from the VtC emission lines. While valence-to-core resonant emission data have been reported,[27–30] to our knowledge there has been no systematic investigation of the ability to perform ligand-selective XAS using valence-to-core detection.

In the present study, we investigated the ability of VtC-detected XAS (i.e., HERFD from VtC features) to impart ligand selectivity to XANES spectra. A series of well-defined manganese nitrido and oxo complexes that possess strong XAS and XES features was chosen for this study. These include $(NMe_4)_2Na[Mn(CN)_5N]\cdot H_2O$,[31] $(PPh_4)_2[Mn(CN)_4N]\cdot 2H_2O$,[31] $PPh_4[Mn(taml)O]$,[32] and $KMnO_4$ (see Scheme 1 for the structures of the metal complexes). For $(NMe_4)_2Na[Mn(CN)_5N]\cdot H_2O$ and $PPh_4[Mn(taml)O]$, polarized Mn K-edge XANES data were previously reported.[10] In the present

Scheme 1. Structures of the Compounds Used in This Study
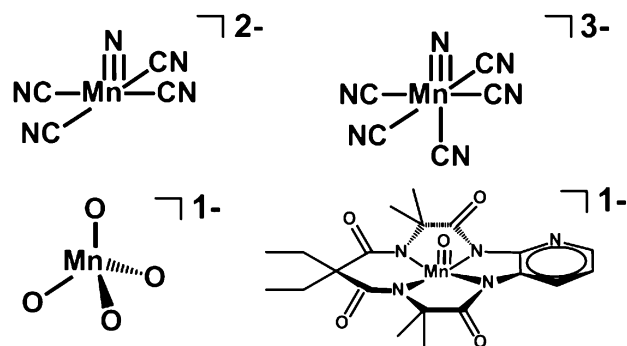
study, we first examined nonresonant XES data on this series of complexes in order to rigorously identify and assign the valence emission features. Standard XAS data, obtained in total fluorescence mode, were also collected as a reference point for the VtC-detected XAS.

With these assignments in place, we then collected full resonant X-ray emission (RXES) planes (Figure 1 and Figure S1 in the Supporting Information). These planes contain information on how the absorption spectrum changes with varying detection energy and can be considered as similar to other two-dimensional spectroscopies (e.g., 2D NMR and 2D IR) whereby the information content is distributed across two dimensions, allowing for further analysis. In particular, these RXES planes allow for the easy identification of appropriate detection energies since a horizontal "cut" through the RXES plane corresponds to a VtC-detected XAS spectrum at a given emission energy.

Using the detection energies determined from the RXES planes, we then collected VtC-detected XAS spectra for this series of compounds. Spectra for each compound were collected from several VtC features, and these showed dramatic modulations in pre-edge intensity that varied depending on the emission energy utilized for detection. From a quantitative analysis of the compounds studied, we have derived some general trends that apply across a range of compounds. Further, we demonstrate that while a simple one-electron density functional theory (DFT) approach can effectively predict standard XAS and nonresonant XES, such a simple approach is not appropriate for VtC-detected XAS. This is attributed to the fact that multiplet and interference effects are not taken into account at this level of theory. Hence, it is clear that new theoretical developments are required for more rigorous interpretation of these spectra. Nonetheless, the pronounced changes observed experimentally demonstrate that VtC-detected XAS has the potential to further the information content and selectivity of XAS data.

■ EXPERIMENTAL SECTION

Sample Preparation. $KMnO_4$ was purchased from Sigma-Aldrich and used without further purification. The following compounds were synthesized according to published procedures: $(NMe_4)_2Na[Mn(CN)_5N]\cdot H_2O$,[31] $(PPh_4)_2[Mn(CN)_4N]\cdot 2H_2O$,[31] and $PPh_4[Mn(taml)O]$[32] (Scheme 1). For X-ray analysis, samples were ground to a fine powder (with boron nitride where necessary), packed into a 1 mm aluminum cell, and sealed with 38 μm Kapton tape. All samples were loaded into a liquid helium cryostat and maintained at a temperature of ~20 K throughout the course of data collection.

XES Measurements. XES data were collected at beamline ID26 of the European Synchrotron Radiation Facility (ESRF) under ring conditions of 200 mA and 6 GeV. A dual-crystal Si(111)
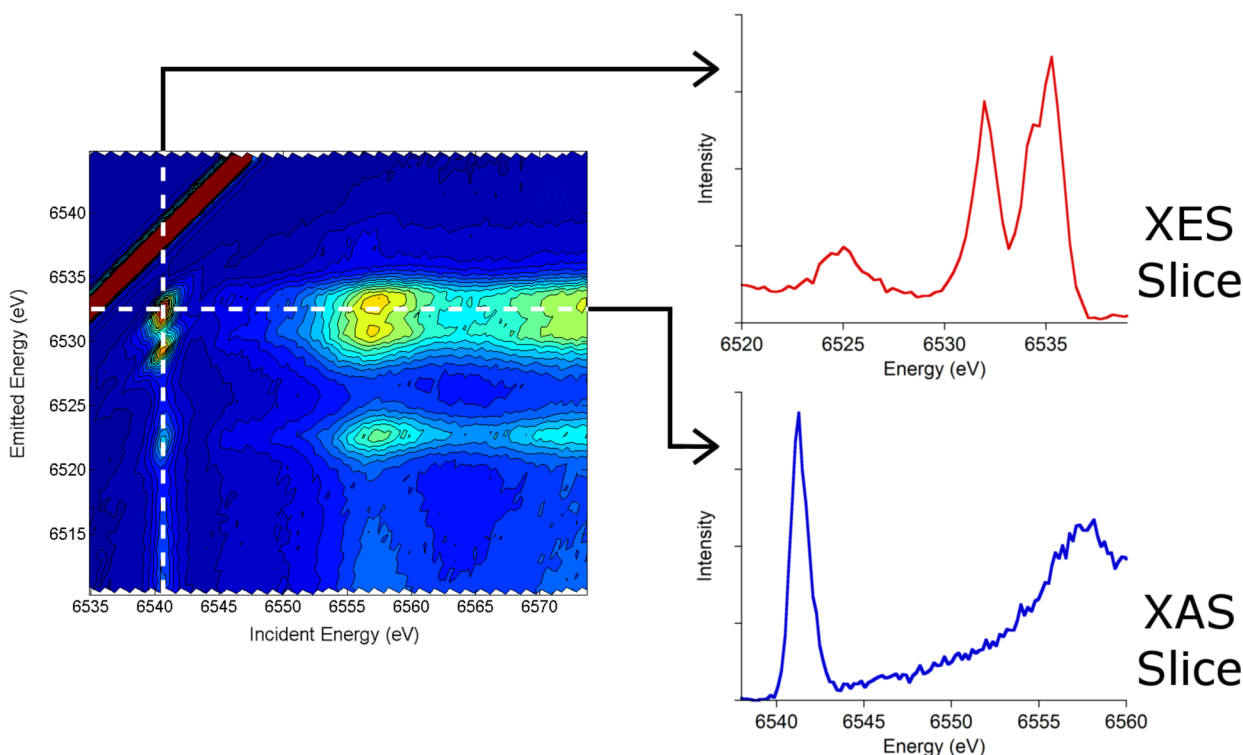
Figure 1. A RXES plane for $[Mn(CN)_4N]^{2-}$ is shown along with "slices" through the plane. A horizontal cut through the plane at constant emitted energy yields a VtC-detected XAS (i.e., HERFD) spectrum, while a vertical slice at constant incident energy gives a resonant X-ray emission spectrum. For clarity, on the displayed plane a two-point binning has been applied to both the incident and emitted energy axes.

monochromator was used upstream for energy selection, and the incident energy was fixed at 6700 eV. The incident flux was $>10^{13}$ photons/s with the beam focused to a spot of 0.25 mm × 1 mm at the sample. Emission spectra were measured using the 440 reflection of five Si crystal analyzers aligned in the Rowland geometry, as described previously.[12,14] An avalanche photodiode detector was used as the X-ray photon detector. Where necessary to prevent sample damage, aluminum filters were inserted before the sample in order to attenuate the incident beam. The energy of the spectrometer was calibrated using a sample of MnO (reference energy values of 6491.68, 6517.71, and 6533.00 eV). The data were normalized with respect to the incident flux using a photodiode upstream of the sample. The space between the sample, the analyzers, and the detector was filled with helium to minimize attenuation of the fluorescence. In order to assess the rate of photoreduction, consecutive short $K\beta_{1,3}$-detected XAS scans were run to determine the acceptable exposure time per sample spot. For all samples, data were obtained from multiple spots, and only those scans that showed no evidence of photoreduction were included in the final averages. Separate scans of the $K\beta$ main line (6475−6505 eV; 0.2 eV step size) and the valence-to-core region (6500−6550 eV; 0.2 eV step size) were obtained. Scans of the $K\beta$ main line and valence-to-core region were separately averaged using PyMCA,[33] and the resultant averages were spliced to form full spectra. The area under each spectrum was set to 1000.

XAS Measurements. XAS data were also collected at beamline ID26 of the ESRF under ring conditions as previously stated. Either a dual-crystal Si(111) or Si(311) monochromator was used upstream for energy selection. The incident fluxes were $>10^{13}$ and $\sim 4 \times 10^{12}$ photons/s with a beam size of 0.1 mm × 1 mm for the Si(111) and Si(311) monochromators, respectively. For data collection, total fluorescence yield (TFY) and VtC-detected XAS spectra were recorded simultaneously. VtC-detected XAS spectra were measured using an array of either five Si(440) or four Ge(440) crystal analyzers aligned on intersecting Rowland circles (vide supra). The energies for the VtC-detected spectra were selected from the RXES planes (vide infra). Aluminum filters were again used where necessary to prevent

sample damage. $KMnO_4$ was used for energy calibration (pre-edge maximum at 6543.3 eV), and the data were normalized to the incident flux. A helium-filled flight path was used to minimize signal attenuation. Damage was assessed as described above, and multiple spots were used for data collection. Near-edge XAS scans were taken over an energy range of 6500−6600 eV in 0.1 eV steps, and for normalization, EXAFS scans were measured over a range of 6500−7000 eV in 0.5 eV steps. These scans were averaged separately using PyMCA, spliced together, and then fit using Blueprint XAS v1.2.[34] Peak positions and areas were identified by fitting pseudo-Voigt peaks to the pre-edge and near-edge regions of the data, and the reported values represent an average of at least 25 reasonable fits. Pre- and post-edge backgrounds (linear or quadratic) were fit during the peak fitting and subsequently subtracted. The spectra were normalized by setting the edge jump equal to 1. Representative fits for all spectra can be found in Figures S2−S5 in the Supporting Information.

RXES Plane Collection. In order to identify how the VtC emission features of these compounds change upon resonant excitation, full RXES planes were collected for each sample, and the energies of the VtC features of interest were identified. The RXES planes were collected by fixing the XES spectrometer to a given energy and then collecting a rapid edge XAS scan at this energy. The spectrometer was then advanced to the next energy and another edge XAS scan was collected on a fresh sample spot. The planes were collected over an XAS energy range of 6535−6575 eV in 0.2 eV steps and an XES energy range of 6510−6545 eV in 0.3 eV steps. Each individual XAS scan was normalized to the total fluorescence signal output to correct for any variation in concentration.

Computations. All of the calculations were carried out using the ORCA version 2.9 or 3.0 quantum-chemical suite.[35] Computations used the BP86 functional[36,37] and the def2-TZVP(-f) basis set[38] with solvation modeled with the conductor-like screening model (COSMO) in an infinite dielectric.[39] Relativistic effects were taken into account using the zeroth-order regular approximation (ZORA)[40] following the model potential implementation of van Wüllen.[41] Crystal structures[31,32,42,43] were used as starting coordinates for geometry

10078

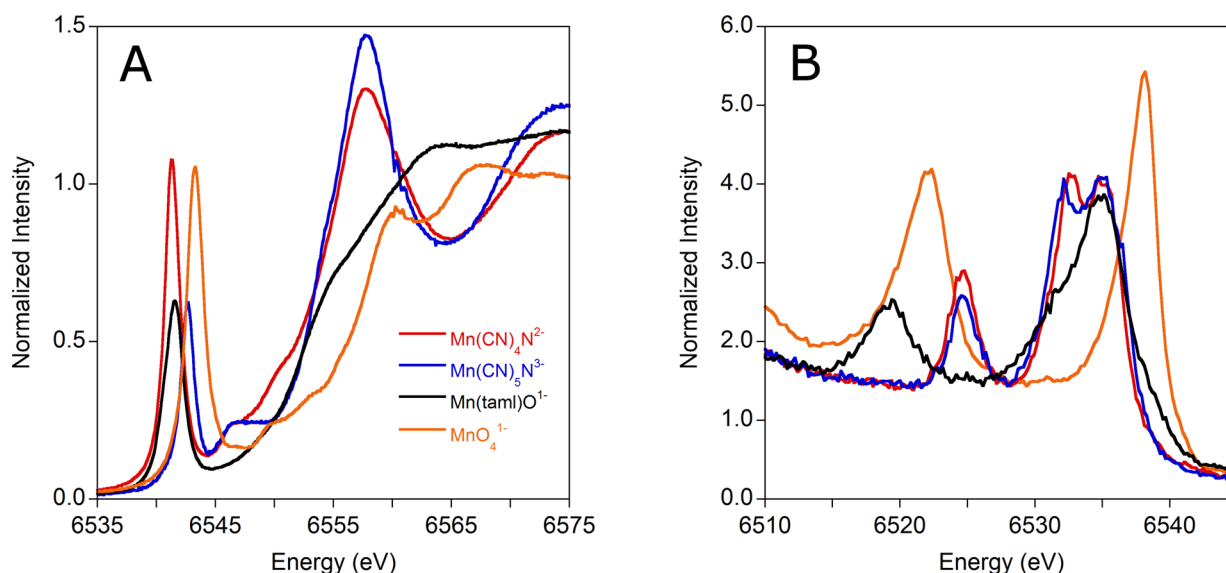dx.doi.org/10.1021/ja504206y | *J. Am. Chem. Soc.* 2014, 136, 10076−10084

Figure 2. TFY XAS spectra (left) and the valence-to-core region of nonresonant XES spectra (right) for the compounds from this study.
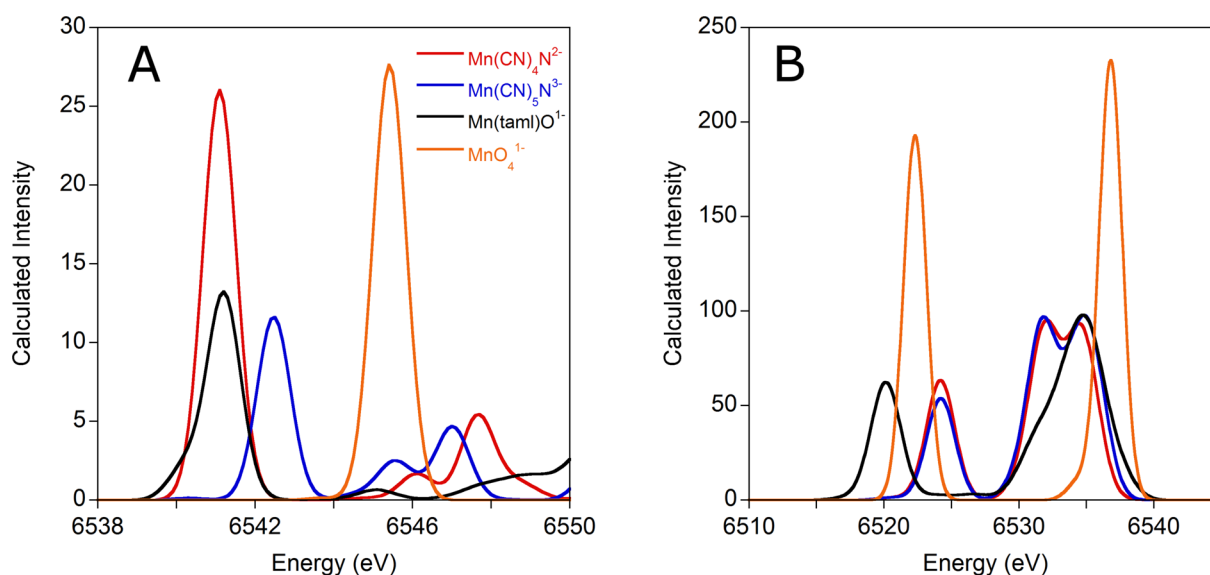

Figure 3. Calculated pre-edge XAS spectra (left) and valence-to-core XES spectra (right) for the compounds studied.

optimizations, and optimized structures were used for all spectral calculations. TFY XAS data were simulated using time-dependent DFT (TD-DFT) calculations (100 roots), and XES spectra were calculated with a simple overlap model according to published procedures;[44] the calculated XAS and XES spectra were broadened by 1.0 and 2.5 eV and shifted by 62.3 and 52.9 eV, respectively. Molecular orbitals were visualized using Chimera.[45]

With this same level of theory, RXES planes were also calculated for all compounds using the one-electron approach implemented in ORCA, as has been done previously.[30] In the simplest sense, these calculations generate RXES planes by convoluting together the one-electron valence-to-core XES and K pre-edge XAS calculations (it should be noted that these XAS calculations are similar to but distinct from the TD-DFT methodology employed to calculate TFY XAS spectra). The implementation in ORCA requires only that the XAS and XES donor orbitals be specified (Mn 1s and all orbitals higher in energy than the Mn 3p, respectively). The RXES planes thus produced have axes in terms of incident energy and energy transfer; to better compare these spectra to experiment, the energy transfer axis was converted to emitted energy by subtraction of the transfer energy from the incident energy. The emitted energy was then calibrated by

applying a scalar shift of 59.2 eV. Rigorous energy calibration for the XAS component of these calculations has not been previously performed, so a scalar shift of 62.7 eV was applied to roughly align this axis with TD-DFT calculations. A sample input file for each calculation is provided in the Supporting Information.

■ RESULTS AND ANALYSIS

TFY XAS and nonresonant XES spectra were recorded for a series of well-characterized Mn compounds (Scheme 1), and their spectra are shown in Figure 2. These spectra very clearly highlight the different and complementary information available from XAS and XES. As a probe of the unoccupied d orbitals, the energies of the XAS pre-edge features are known to be sensitive to the strength of the ligand field.[3] This is evident experimentally as the two five-coordinate Mn(V) compounds have pre-edges at very similar energies while the six-coordinate Mn(V) compound's pre-edge lies ~1 eV to higher energy. The higher-energy pre-edge of MnO_4^- stems from the fact that the manganese ion in this complex is formally Mn(VII), resulting in

a lower-energy 1s orbital and thus greater pre-edge and edge transition energies. Additionally, symmetry effects can be seen to affect the intensity of the pre-edge, with the clearest example provided by the two nitrides. The addition of an axial cyanide ligand in $[Mn(CN)_5N]^{3-}$ partially restores centrosymmetry relative to $[Mn(CN)_4N]^{2-}$, attenuating the mechanism for p−d mixing and therefore reducing the intensity of the pre-edge.[42] Further highlighted by these spectra is the lack of sensitivity to ligand identity, with the pre-edge features of $[Mn(CN)_4N]^{2-}$ and $[Mn(taml)O]^{1-}$ having identical pre-edge energies despite the fact that these compounds have very different axial and supporting ligands.

Conversely, XES probes the occupied orbitals of a metal complex. Both the low-energy $K\beta''$ (ligand ns to metal 1s) and higher-energy $K\beta_{2,5}$ features (ligand np and intraligand ns σ^* orbitals to metal 1s) are known to have a high degree of ligand sensitivity.[12−15] As shown in Figure 2B, the $K\beta''$ peak (at ∼6519 to 6525 eV) shifts ∼6 eV to higher energy for the Mn(V) complexes on going from an oxo to a nitride, reflecting the difference in ligand 2s ionization potentials. It should be noted that the $K\beta''$ peak of MnO_4^- falls ∼3 eV to higher energy than $[Mn(taml)]O^{1-}$, even though both are dominantly O 2s features. As in the XAS, this shift reflects the greater stability of the Mn 1s orbital for Mn(VII) relative to Mn(V).

To higher energy lie the $K\beta_{2,5}$ emission features, which for permanganate can simply be assigned as transitions from the O 2p orbitals; similarly, the nitride features may be assigned as deriving almost exclusively from intracyanide 2s2s σ^* orbitals (the ∼6532 eV feature) and a mixture of nitride 2p and intracyanide 2p2p σ orbitals (the ∼6535 eV peak). The assignment of the single peak present for $[Mn(taml)O]^{1-}$ to specific ligand contributions is prohibited by the overlap of numerous ligand-2p-derived transitions from both the taml macrocycle and the oxo O 2p orbitals. Nonetheless, the distinct electronic structures of the supporting ligands in these complexes give rise to significant differences in the VtC XES spectra.

Support for these assignments is provided by simple DFT calculations of the XAS and XES spectra for this series, as shown in Figure 3 and in Figures S6−S9 in the Supporting Information. The generally good agreement between experiment and theory, seen clearly by comparison of Figures 2 and 3, allows us to use the calculated spectra to assign the observed transitions. In short, the XAS pre-edge of $[Mn(CN)_4N]^{2-}$ is dominated by a single transition to an orbital with contributions from the Mn $3d_{z^2}$ and N $2p_z$ orbitals; the large XAS intensity is conferred via significant mixing of Mn $4p_z$ character (∼11%) (Figure S6). The three valence-to-core features derive from transitions from the nitride 2s orbital, the cyanide 2s2s σ^* orbital, and a mixture of nitride 2p and cyanide $2p_z2p_z$ σ bonding orbitals, respectively, all with small but appreciable Mn np mixing. Similar assignments for the remaining compounds can be found in Figures S7−S9, and a full discussion of how these were obtained is provided in ref 15.

The detailed assignments of these nonresonant spectra are crucial as they allow for rational selection of detection energies according to VtC transition character. If one were to think about these spectra in a manner analogous to resonance Raman spectra, enhancement of a given XAS feature could be obtained by detecting from an emission feature of similar character. For example, if enhancement of the pre-edge of $[Mn(CN)_4N]^{2-}$ were desired, this effect might be achieved by detection from a valence-to-core feature with significant nitride character.

With these assignments in hand, the experimental collection of XAS spectra from VtC features can be done similarly to a $K\alpha$ HERFD measurement: the emission spectrometer can be set to the energy of a given valence-to-core feature—the $K\beta''$ feature, for example—and the incident energy varied to obtain an XAS spectrum. Employing such a methodology has been previously suggested as a means to impart ligand selectivity to XAS spectra.[11] The explicit detection energies chosen and the XES features to which they correspond are given in Table 1.

**Table 1. Detection Energies (eV) Chosen for VtC-Detected XAS Spectra**

complex	$K\beta''$	$K\beta_{2,5}$ (1)	$K\beta_{2,5}$ (2)
$[Mn(CN)_4N]^{2-}$	6524.1	6531.4	6534.5
$[Mn(CN)_5N]^{3-}$	6523.5	6530.7	6533.5
$[Mn(taml)O]^{1-}$	6518.6	6534.8	
MnO_4^{1-}	6521.7	6536.8	

It is noted that the energies of the valence-to-core emission features will change under resonant conditions as, instead of being fully ionized, the Mn 1s electron remains bound and localized on the metal. This more stable intermediate state results in slightly lower energy emission features. To account for these small variable shifts, RXES planes (Figure 1 and Figure S1 in the Supporting Information) for all of the samples were collected, and the energies of the different valence-to-core emission features were selected from these planes (e.g., as shown by the dashed line in Figure 1).

Figure 4 shows the resulting VtC-detected XAS spectra for the Mn model compounds, and Table 2 gives the normalized areas of the pre-edge regions for each (intensity-weighted average energies and percentage enhancements are provided in Tables S1 and S2 in the Supporting Information, respectively). As shown clearly by the data in Figure 4 and Table 2, significant changes in the absolute pre-edge intensities—both increases and decreases—are seen when detecting XAS from different emission features. Importantly, this effect is distinct from the well-known line sharpening due to decreased lifetime broadening, which would increase the apparent peak *height*[46] but not increase the peak *area*. Indeed, for all of the compounds studied, increases in pre-edge area ranging from 5% to 62% were observed when detecting from the $K\beta_{2,5}$ features. Conversely, detection from the $K\beta''$ peaks yielded reductions in the pre-edge intensity (−18% to −33%) for all of the compounds except $KMnO_4$, for which a modest increase of 10% was seen. These intensity modulations are not, however, accompanied by significant energetic shifts, suggesting that the same electronic transitions are operative for the various detection energies.

It should be noted that the degree of enhancement observed for each VtC feature is strongly dependent on the detection energy used. Figure S10 in the Supporting Information demonstrates that changes in detection energy as small as 0.3 eV can result in noticeable intensity variations. Thus, care must be taken both when selecting the exact detection energy and also when comparing spectra obtained at slightly different energies.

Lastly, spectra obtained by detection from the low-energy $K\beta_{2,5}$ feature of the nitrides show the appearance of new features to lower energy from the main pre-edge peak. Rather than deriving from new electronic transitions, these features appear to emerge from "bleeding" of the lifetime broadening of
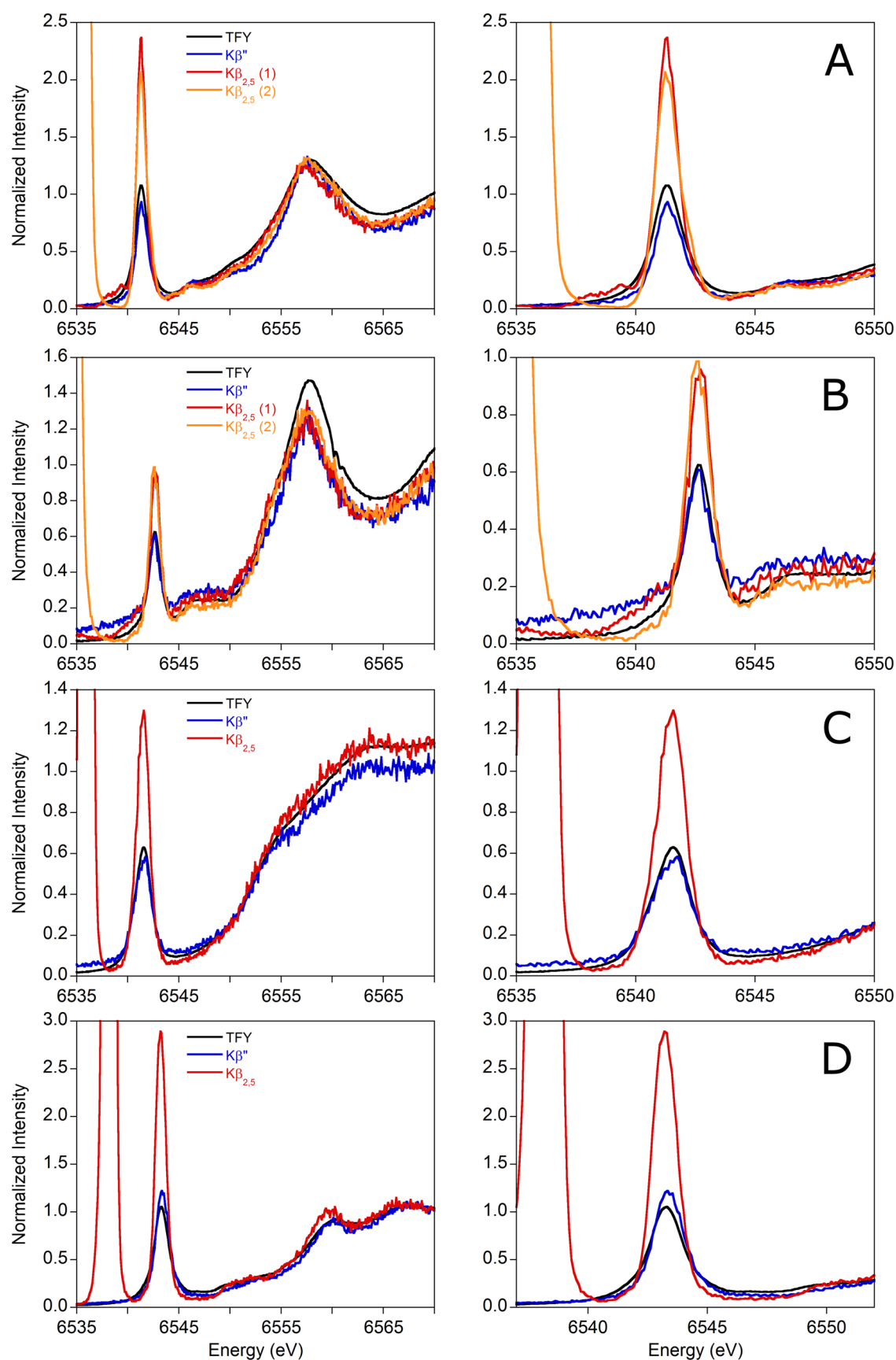
Figure 4. Overlays of TFY and VtC-detected XAS spectra for (A) $[Mn(CN)_4N]^{2-}$, (B) $[Mn(CN)_5N]^{3-}$, (C) $[Mn(taml)O]^{1-}$, and (D) MnO_4^{1-}. Expansions of the pre-edge regions are shown to the right. The exact energies of detection are given in Table 1. The high-intensity peak visible at the lowest energies for some spectra is due to elastic scatter of the incident beam.

10081

dx.doi.org/10.1021/ja504206y | *J. Am. Chem. Soc.* 2014, 136, 10076−10084

Table 2. Normalized Areas for VtC-Detected XAS Spectra[a]

	TFY	$K\beta''$	$K\beta_{2,5}$ (1)	$K\beta_{2,5}$ (2)
$[Mn(CN)_4N]^{2-}$	235 (3)	175 (5)	353 (5)	280 (3)
$[Mn(CN)_5N]^{3-}$	131 (5)	87 (7)	137 (6)	158 (4)
$[Mn(taml)O]^{1-}$	160 (3)	131 (4)	230 (6)	
MnO_4^{1-}	251 (6)	275 (11)	408 (12)	

[a]Numbers in parentheses are the standard deviations of the reported values.

the high-energy $K\beta_{2,5}$ peak into the HERFD cut at lower energy (in RXES spectra displayed as they are here, the lifetime broadenings are dispersed along the diagonal).[46] The observation of these additional peaks is a strong motivator for collecting entire RXES planes when attempting to analyze HERFD data so as to enable the identification of these features.

Taken together, these data are perhaps somewhat surprising. In a simple picture, one might expect the greatest pre-edge enhancement when detecting from valence-to-core features with the most axial ligand character. This is due to the fact that the pre-edge features in the TFY XAS spectra are known to be dominated by interactions between the Mn 3d/4p orbitals and the 2p orbitals of the axial ligand. Specifically, metal–ligand covalency has been shown to mediate metal 3d–4p mixing, providing a mechanism for intense pre-edges in metal–oxo and metal–nitrido complexes.[10] Interestingly, for the nitrides, the largest increase in pre-edge intensity was observed when detecting XAS from the emission lines dominated by the cyanide supporting ligands, while for all of the compounds, detection from the axial-ligand-dominated $K\beta''$ line resulted in negative or small positive enhancements. This may to some extent reflect the relative involvement of ligand 2s versus 2p orbitals in bonding and their ability to mediate 3d–4p mixing. It should also be noted that these spectra have all been normalized to the intensity of the continuum ionization at high energy, so the observed pre-edge changes are *relative* to this intensity. Thus, the observed differences may reflect the extent to which the ligand 2s and 2p orbitals hybridize with and mediate mixing between metal 3d and 4p orbitals. Nonetheless, it is clear that detecting XAS spectra from valence-to-core features imparts large observable changes in the experimental spectra.

Because the DFT calculations effectively reproduced the standard XAS and XES spectra, we also attempted to calculate the RXES planes and VtC-detected XAS spectra to better understand the observed effects. The calculated planes can be found in Figure 5 and Figure S11 in the Supporting Information. An initial inspection of the planes reveals that all of the observed experimental features are reproduced with relatively accurate energies and energetic splittings. Thus, from a qualitative inspection of the entire plane, these calculations do an acceptable job of reproducing the experimental data.

A closer look, however, uncovers severe flaws in these one-electron calculations. For example, taking cuts through the calculated plane for $[Mn(CN)_4N]^{2-}$ to generate VtC-detected XAS spectra followed by normalization to the 1s to 4p transition intensity fails to reproduce the experimental modulations in pre-edge intensity (Figure 6). Indeed, the calculated pre-edges all have almost identical intensities. Furthermore, experimentally it is observed that the relative intensities of the XES features—particularly the $K\beta''$ peak— change dramatically depending on the excitation energy used.
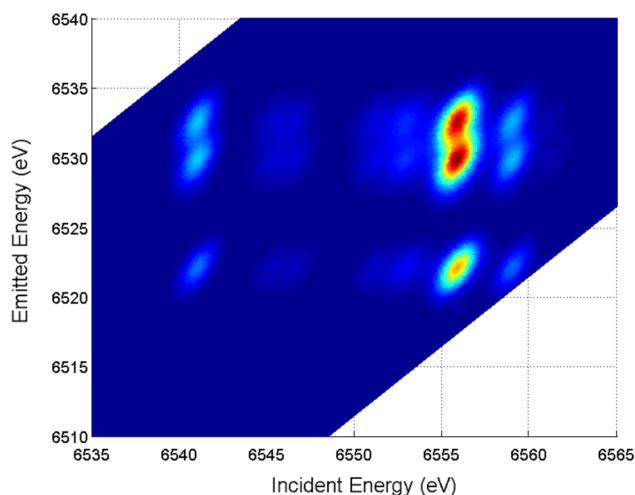

Figure 5. A RXES plane calculated for $[Mn(CN)_4N]^{2-}$ using the one-electron implementation in ORCA.

This effect is also not reproduced by the calculations (Figure 6).

These calculations have previously been noted as adequately reproducing experiment,[30] and from a qualitative view of the entire plane they do capture the presence of the major features. What they do not capture, however, are the intensity modulations and appearance of new low-intensity features seen in the present set of experiments. As the present calculations inherently neglect the three-state nature of these experiments as well as the presence of multiplet and interference effects, this is perhaps not surprising. Attempting to approximate some of these effects, such as via a ROCIS procedure,[47] may yield significant improvement, though clearly additional theoretical developments are needed in order to capture the physics governing the intensity modulations observed here. These investigations are ongoing in our laboratory.

■ CONCLUSIONS

In this study, a series of well-characterized manganese model compounds were investigated by TFY XAS, nonresonant XES, and valence-to-core-detected XAS. The TFY XAS spectra demonstrated a sensitivity to metal site symmetry and ligand field strength, while the VtC XES spectra were most affected by ligand identity and electronic structure. Thus, these "standard" spectra were shown to contain unique and complementary information about these complexes. Straightforward DFT calculations reproduced the experimental spectra very well and confirmed the spectral assignments obtained from ligand field and molecular orbital theory arguments.

By combining these experiments and detecting XAS spectra from VtC XES features, significant (−33% to +62%) pre-edge intensity modulations were observed relative to the standard TFY spectra. These modulations included universal large intensity enhancements when detecting from the $K\beta_{2,5}$ peaks and (except for $KMnO_4$) decreases in intensity when detecting from the $K\beta''$ peaks that cannot be explained solely by changes in lifetime broadenings. Furthermore, additional peaks were observed in some of the $K\beta_{2,5}$-detected XAS spectra of the nitrides that were attributed to the lifetime broadenings of nearby features. These observations could not be reproduced by one-electron DFT calculations, indicating that additional
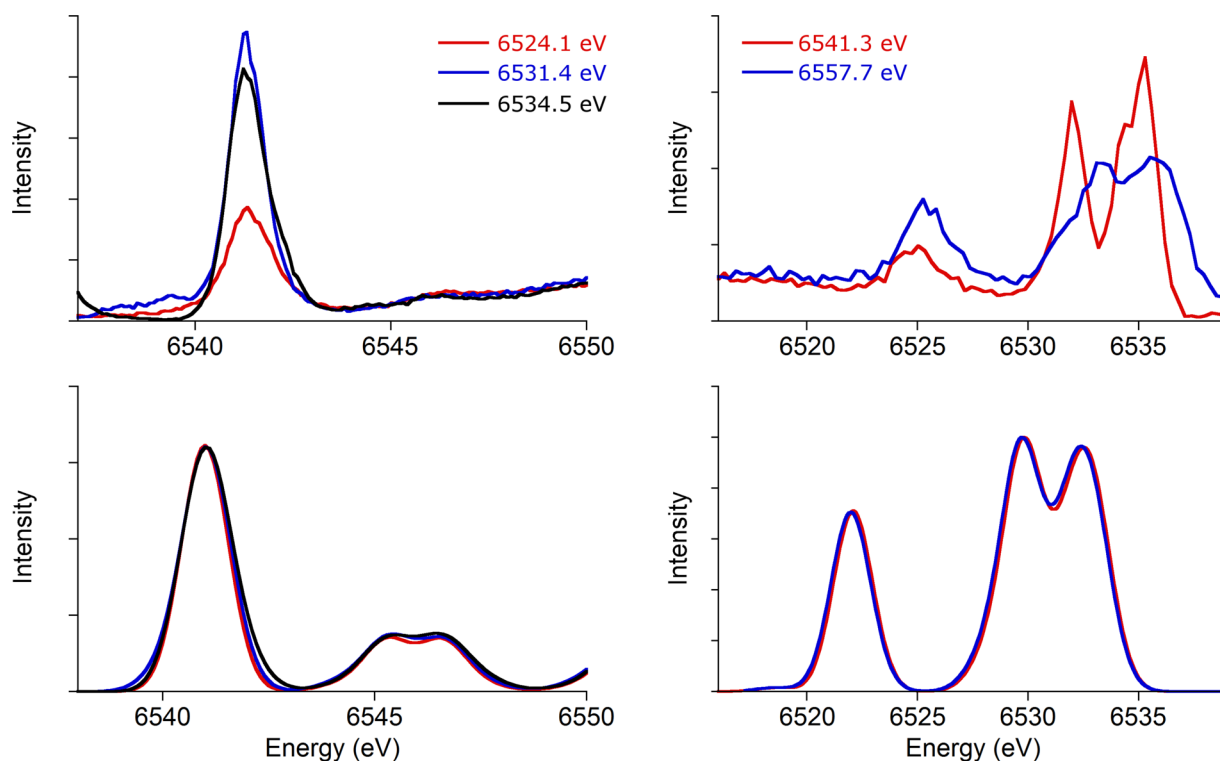
Figure 6. Comparison between experimental and calculated VtC-detected XAS (left) and resonant XES (right) data for $[Mn(CN)_4N]^{2-}$. The experimental spectra are shown at the top and the calculated ones on the bottom; the labels indicate the energies from which the experimental spectra were measured. The calculated slices were taken from the corresponding features in the computed spectra. The significant experimental changes in the spectra are not reproduced in the calculations.

theoretical developments are needed in order to properly treat these spectra.

While the exact physical mechanisms underpinning these spectra remain elusive, the extent to which the pre-edge areas can be modulated demonstrates that further investigation is warranted. A better understanding of these mechanisms may very well establish VtC-detected XAS as a step forward on the path toward ligand-selective XAS spectra.

■ ASSOCIATED CONTENT

ⓢ Supporting Information

Full experimental RXES planes for all compounds, representative fits and numerical data for all TFY and VtC-detected XAS spectra, spectral assignments for all calculated XAS and XES spectra, plot of sequential RXES slices showing the impact of detection energy on pre-edge intensity, calculated RXES planes for all compounds, ORCA input files, and *xyz* coordinates for optimized structures. This material is available free of charge via the Internet at http://pubs.acs.org.

■ AUTHOR INFORMATION

Corresponding Author

serena.debeer@cec.mpg.de

Present Address

∇C.J.P.: Department of Chemistry, The Pennsylvania State University, University Park, PA 16802, United States.

Notes

The authors declare no competing financial interest.

■ REFERENCES

(1) Singh, J.; Lamberti, C.; van Bokhoven, J. A. *Chem. Soc. Rev.* **2010**, *39*, 4754−4766.

(2) de Groot, F. M. F.; Kotani, A. *Core Level Spectroscopy of Solids*; CRC Press: Boca Raton, FL, 2008.

(3) Westre, T. E.; Kennepohl, P.; DeWitt, J. G.; Hedman, B.; Hodgson, K. O.; Solomon, E. I. *J. Am. Chem. Soc.* **1997**, *119*, 6297−6314.

(4) Penner-Hahn, J. E. *Coord. Chem. Rev.* **1999**, *190−192*, 1101−1123.

(5) Shu, L. J.; Nesheim, J. C.; Kauffmann, K.; Münck, E.; Lipscomb, J. D.; Que, L., Jr. *Science* **1997**, *275*, 515−518.

(6) Messinger, J.; Robblee, J. H.; Bergmann, U.; Fernandez, C.; Glatzel, P.; Visser, H.; Cinco, R. M.; McFarlane, K. L.; Bellacchio, E.; Pizarro, S. A.; Cramer, S. P.; Sauer, K.; Klein, M. P.; Yachandra, V. K. *J. Am. Chem. Soc.* **2001**, *123*, 7804−7820.

(7) Penner-Hahn, J. E. *Coord. Chem. Rev.* **2005**, *249*, 161−177.

(8) Pickering, I. J.; George, G. N. *Inorg. Chem.* **1995**, *34*, 3142−3152.

(9) Hahn, J. E.; Scott, R. A.; Hodgson, K. O.; Doniach, S.; Desjardins, S. R.; Solomon, E. I. *Chem. Phys. Lett.* **1982**, *88*, 595−598.

(10) Yano, J.; Robblee, J.; Pushkar, Y.; Marcus, M. A.; Bendix, J.; Workman, J. M.; Collins, T. J.; Solomon, E. I.; DeBeer George, S.; Yachandra, V. K. *J. Am. Chem. Soc.* **2007**, *129*, 12989−13000.

(11) de Groot, F. *Chem. Rev.* **2001**, *101*, 1779−1808.

(12) Glatzel, P.; Bergmann, U. *Coord. Chem. Rev.* **2005**, *249*, 65−95.

10083

dx.doi.org/10.1021/ja504206y | *J. Am. Chem. Soc.* 2014, 136, 10076−10084

(13) Bergmann, U.; Horne, C. R.; Collins, T. J.; Workman, J. M.; Cramer, S. P. *Chem. Phys. Lett.* **1999**, *302*, 119−124.

(14) Lee, N.; Petrenko, T.; Bergmann, U.; Neese, F.; DeBeer, S. *J. Am. Chem. Soc.* **2010**, *132*, 9715−9727.

(15) Pollock, C. J.; DeBeer, S. *J. Am. Chem. Soc.* **2011**, *133*, 5594−5601.

(16) Lassalle-Kaiser, B.; Boron, T. T.; Krewald, V.; Kern, J.; Beckwith, M. A.; Delgado-Jaime, M. U.; Schroeder, H.; Alonso-Mori, R.; Nordlund, D.; Weng, T.-C.; Sokaras, D.; Neese, F.; Bergmann, U.; Yachandra, V. K.; DeBeer, S.; Pecoraro, V. L.; Yano, J. *Inorg. Chem.* **2013**, *52*, 12915−12922.

(17) Kropp, H.; King, A. E.; Khusniyarov, M. M.; Heinemann, F. W.; Lancaster, K. M.; DeBeer, S.; Bill, E.; Meyer, K. *J. Am. Chem. Soc.* **2012**, *134*, 15538−15544.

(18) Hämäläinen, K.; Siddons, D. P.; Hastings, J. B.; Berman, L. E. *Phys. Rev. Lett.* **1991**, *67*, 2850−2853.

(19) Hämäläinen, K.; Kao, C. C.; Hastings, J. B.; Siddons, D. P.; Berman, L. E.; Stojanoff, V.; Cramer, S. P. *Phys. Rev. B* **1992**, *46*, 14274−14277.

(20) Peng, G.; de Groot, F. M. F.; Hämäläinen, K.; Moore, J. A.; Wang, X.; Grush, M. M.; Hastings, J. B.; Siddons, D. P.; Armstrong, W. H.; Mullins, O. C.; Cramer, S. P. *J. Am. Chem. Soc.* **1994**, *116*, 2914−2920.

(21) Wang, X.; Grush, M. M.; Froeschner, A. G.; Cramer, S. P. *J. Synchrotron Radiat.* **1997**, *4*, 236−242.

(22) Peng, G.; Wang, X.; Randall, C. R.; Moore, J. A.; Cramer, S. P. *Appl. Phys. Lett.* **1994**, *65*, 2527−2529.

(23) Wang, X.; de Groot, F. M. F.; Cramer, S. P. *Phys. Rev. B* **1997**, *56*, 4553−4564.

(24) Tsutsumi, K.; Nakamori, H.; Ichikawa, K. *Phys. Rev. B* **1976**, *13*, 929−933.

(25) Gamblin, S. D.; Urch, D. S. *J. Electron Spectrosc. Relat. Phenom.* **2001**, *113*, 179−192.

(26) Glatzel, P.; Jacquamet, L.; Bergmann, U.; de Groot, F. M. F.; Cramer, S. P. *Inorg. Chem.* **2002**, *41*, 3121−3127.

(27) Leidel, N.; Chernev, P.; Havelius, K. G. V.; Ezzaher, S.; Ott, S.; Haumann, M. *Inorg. Chem.* **2012**, *51*, 4546−4559.

(28) Gallo, E.; Lamberti, C.; Glatzel, P. *Inorg. Chem.* **2013**, *52*, 5633−5635.

(29) Meyer, D. A.; Zhang, X.; Bergmann, U.; Gaffney, K. J. *J. Chem. Phys.* **2010**, *132*, No. 134502.

(30) Gallo, E.; Bonino, F.; Swarbrick, J. C.; Petrenko, T.; Piovano, A.; Bordiga, S.; Gianolio, D.; Groppo, E.; Neese, F.; Lamberti, C.; Glatzel, P. *ChemPhysChem* **2013**, *14*, 79−83.

(31) Bendix, J.; Meyer, K.; Weyhermüller, T.; Bill, E.; Metzler-Nolte, N.; Wieghardt, K. *Inorg. Chem.* **1998**, *37*, 1767−1775.

(32) Miller, C. G.; Gordon-Wylie, S. W.; Horwitz, C. P.; Strazisar, S. A.; Peraino, D. K.; Clark, G. R.; Weintraub, S. T.; Collins, T. J. *J. Am. Chem. Soc.* **1998**, *120*, 11540−11541.

(33) Sole, V. A.; Papillon, E.; Cotte, M.; Walter, P.; Susini, J. *Spectrochim. Acta, Part B* **2007**, *62*, 63−68.

(34) Delgado-Jaime, M. U.; Mewis, C. P.; Kennepohl, P. *J. Synchrotron Radiat.* **2010**, *17*, 132−137.

(35) Neese, F. *Wiley Interdiscip. Rev.: Comput. Mol. Sci.* **2012**, *2*, 73−78.

(36) Becke, A. D. *Phys. Rev. A* **1988**, *38*, 3098−3100.

(37) Perdew, J. P. *Phys. Rev. B* **1986**, *33*, 8822−8824.

(38) Pantazis, D. A.; Chen, X. Y.; Landis, C. R.; Neese, F. *J. Chem. Theory Comput* **2008**, *4*, 908−919.

(39) Klamt, A.; Schüürmann, G. *J. Chem. Soc., Perkin. Trans. 2* **1993**, 799−805.

(40) van Lenthe, E.; van der Avoird, A.; Wormer, P. E. S. *J. Chem. Phys.* **1998**, *108*, 4783−4796.

(41) van Wüllen, C. *J. Chem. Phys.* **1998**, *109*, 392−399.

(42) Bendix, J.; Deeth, R. J.; Weyhermüller, T.; Bill, E.; Wieghardt, K. *Inorg. Chem.* **2000**, *39*, 930−938.

(43) Karaman, H.; Barton, R. J.; Robertson, B. E.; Lee, D. G. *J. Org. Chem.* **1984**, *49*, 4509−4516.

(44) Beckwith, M. A.; Roemelt, M.; Collomb, M.-N.; DuBoc, C.; Weng, T.-C.; Bergmann, U.; Glatzel, P.; Neese, F.; DeBeer, S. *Inorg. Chem.* **2011**, *50*, 8397−8409.

(45) Pettersen, E. F.; Goddard, T. D.; Huang, C. C.; Couch, G. S.; Greenblatt, D. M.; Meng, E. C.; Ferrin, T. E. *J. Comput. Chem.* **2004**, *13*, 1605−1612.

(46) Glatzel, P.; Sikora, M.; Fernández-García, M. *Eur. Phys. J.: Spec. Top.* **2009**, *169*, 207−214.

(47) Roemelt, M.; Maganas, D.; DeBeer, S.; Neese, F. *J. Chem. Phys.* **2013**, *138*, No. 204101.